Formation of moiré interlayer excitons in space and time

Article

Formation of moiré interlayer excitons in space and time

https://doi.org/10.1038/s41586-022-04977-7

Received: 5 November 2021

Accepted: 14 June 2022

Published online: 17 August 2022

Check for updates

David Schmitt[1], Jan Philipp Bange[1], Wiebke Bennecke[1], AbdulAziz AlMutairi[2], Giuseppe Meneghini[3], Kenji Watanabe[4], Takashi Taniguchi[5], Daniel Steil[1], D. Russell Luke[6], R. Thomas Weitz[1,7], Sabine Steil[1], G. S. Matthijs Jansen[1], Samuel Brem[3], Ermin Malic[3,8], Stephan Hofmann[2], Marcel Reutzel[1]✉ & Stefan Mathias[1,7]✉

Moiré superlattices in atomically thin van der Waals heterostructures hold great promise for extended control of electronic and valleytronic lifetimes[1–7], the confinement of excitons in artificial moiré lattices[8–13] and the formation of exotic quantum phases[14–18]. Such moiré-induced emergent phenomena are particularly strong for interlayer excitons, where the hole and the electron are localized in different layers of the heterostructure[19,20]. To exploit the full potential of correlated moiré and exciton physics, a thorough understanding of the ultrafast interlayer exciton formation process and the real-space wavefunction confinement is indispensable. Here we show that femtosecond photoemission momentum microscopy provides quantitative access to these key properties of the moiré interlayer excitons. First, we elucidate that interlayer excitons are dominantly formed through femtosecond exciton–phonon scattering and subsequent charge transfer at the interlayer-hybridized Σ valleys. Second, we show that interlayer excitons exhibit a momentum fingerprint that is a direct hallmark of the superlattice moiré modification. Third, we reconstruct the wavefunction distribution of the electronic part of the exciton and compare the size with the real-space moiré superlattice. Our work provides direct access to interlayer exciton formation dynamics in space and time and reveals opportunities to study correlated moiré and exciton physics for the future realization of exotic quantum phases of matter.

The advent of two-dimensional van der Waals materials[21] has led to remarkable strategies to manipulate correlated material properties. In transition-metal dichalcogenides (TMDs), exceptional light–matter coupling and weak Coulomb screening of photoexcited electron–hole pairs allows the realization of novel spin, valley and excitonic properties of matter[22,23]. Even more intriguing material properties can be accomplished in TMDs by stacking several monolayers into heterostructures[19,20,24]. In type II band-aligned stacks, novel excitonic states can be created, where the electron and the hole contribution to the exciton are separated between the van der Waals-coupled TMDs[13] (Fig. 1e). A key question that remains unanswered is how these interlayer excitons (ILXs) are formed. Furthermore, the lattice mismatch and the twist angle between the TMDs induce a moiré superlattice, which makes it necessary to understand how precisely the interaction of the exciton and the moiré potential determines the material properties (Fig. 1d). Most intriguingly, it has been shown by optical[10–12] and momentum microscopy[13] experiments that ILXs can be confined within the moiré potential minima. However, a substantial open challenge is the experimental identification of universal hallmarks that indicate signatures of the moiré superlattice imprinted onto the ILX.

Experimental quantitative insight into the ILX formation process and the influence of moiré modulation on the ILX is currently limited. All-optical spectroscopy techniques are sensitive only to transitions within the light cone[25] and thus lack the momentum information that is necessary to gain access to the time-dependent energy–momentum fingerprints of the probed quasiparticles[26–28]. Using multidimensional time- and angle-resolved photoelectron spectroscopy (trARPES) on a tungsten diselenide/molybdenum disulfide (WSe_2/MoS_2) heterostructure, we experimentally find that ILXs are dominantly formed through exciton–phonon scattering via intermediate dark excitonic states at the Σ valleys of the hexagonal Brillouin zones. These results are fully supported by a microscopic model including exciton–light and exciton–phonon interaction on a microscopic footing. Furthermore, we observe a complex momentum fingerprint of the ILX, and we show that this fingerprint is a direct hallmark signature of the moiré

[1]I. Physikalisches Institut, Georg-August-Universität Göttingen, Göttingen, Germany. [2]Department of Engineering, University of Cambridge, Cambridge, UK. [3]Fachbereich Physik, Philipps-Universität, Marburg, Germany. [4]Research Center for Functional Materials, National Institute for Materials Science, Tsukuba, Japan. [5]International Center for Materials Nanoarchitectonics, National Institute for Materials Science, Tsukuba, Japan. [6]Institute for Numerical and Applied Mathematics, Georg-August-Universität Göttingen, Göttingen, Germany. [7]International Center for Advanced Studies of Energy Conversion (ICASEC), University of Göttingen, Göttingen, Germany. [8]Department of Physics, Chalmers University of Technology, Gothenburg, Sweden. ✉e-mail: marcel.reutzel@phys.uni-goettingen.de; smathias@uni-goettingen.de

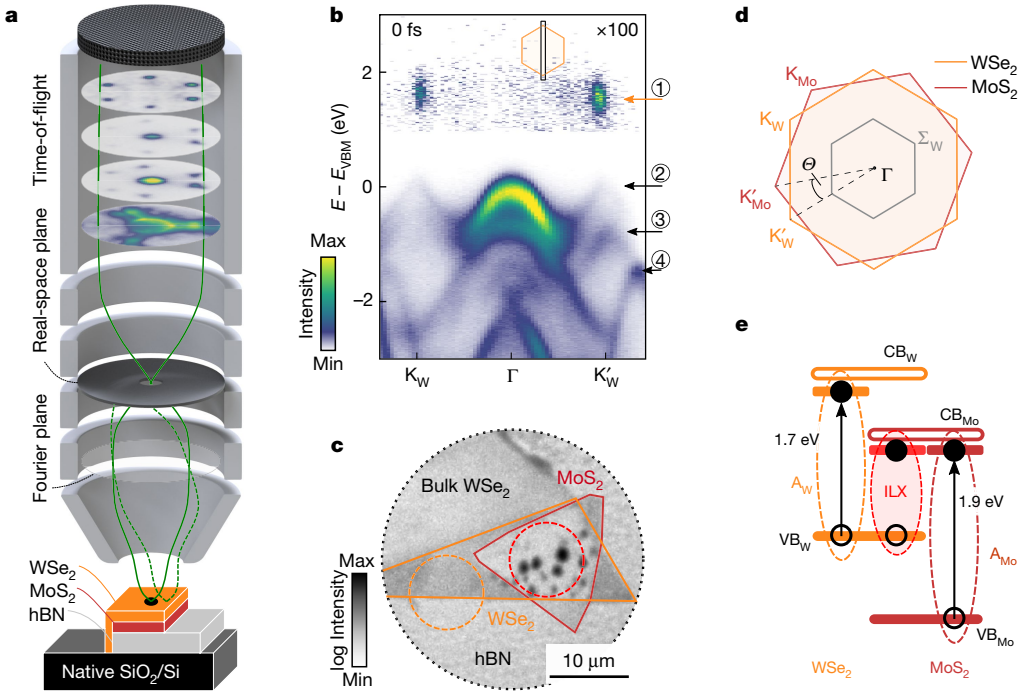

Fig. 1 | Inter- and intralayer excitons in WSe_2/MoS_2 probed by femtosecond momentum microscopy. a, Illustration of the experimental set-up and the WSe_2/MoS_2/hBN sample. **b**, The valence bands of WSe_2 (2), MoS_2 (3) and hBN (4) are labelled in the energy–momentum cut. At 0 fs, bright A_W excitons (1) are detected at the K_W and K'_W valleys of WSe_2. **c**, The heterostructure can be identified in the real-space mode of the microscope. The WSe_2/MoS_2 and WSe_2 regions of interest are indicated by red and orange circles, respectively (10-μm diameter; Methods). **d**, The hexagonal Brillouin zones of WSe_2 (orange) and MoS_2 (dark red) are misaligned by a twist angle Θ. **e**, Bright A_W and A_{Mo} excitons of WSe_2 (orange) and MoS_2 (dark red) can be resonantly excited with 1.7-eV and 1.9-eV pump photons, respectively (VB_W and VB_{Mo}, valence-band maxima; CB_W and CB_{Mo}, conduction-band minima). The hole and the electron contribution of the ILX resides in the WSe_2 and MoS_2 layers, respectively.

superlattice modification. From this data, we then reconstruct the real-space wavefunction probability density of the electronic part of the exciton's wavefunction, which we compare with the moiré superlattice size.

Electronic band structure of WSe_2/MoS_2

We focus our study on the model system WSe_2/MoS_2 with a twist angle of 9.8 ± 0.8° (Extended Data Figs. 1 and 4)[29] and use our customized trARPES system that combines a momentum microscope[30] with a high-repetition-rate high-harmonic generation beamline (Fig. 1a and Methods)[31,32]. The 100-μm² heterobilayer region can be identified in the real-space distribution of the measured photoelectron yield (Fig. 1c and Extended Data Fig. 1e,f). By placing an aperture into the real-space image plane of the microscope (red circle in Fig. 1c), we can selectively probe the occupied band structure of WSe_2/MoS_2. The sample quality is evidenced by the sharp spectral features of the occupied electronic structure and the signature of interlayer hybridization of the valence bands of WSe_2 and MoS_2 at the Γ valley[33] (Fig. 1b, energy resolution of about 200 meV; Extended Data Figs. 2 and 3).

Femtosecond ILX formation dynamics

We follow the build-up process of the ILX by resonantly exciting the optically bright A_W exciton of WSe_2 with 1.7 eV, 50 ± 5 fs pulses and study the subsequent ILX formation via photoemission with 26.5 eV, 21 ± 5 fs extreme ultraviolet (XUV) probe pulses (see Extended Data Fig. 5 for spectral assignment of the valence and conduction bands and the WSe_2 and MoS_2 A excitons). Figure 2a shows the highest spectral weight for the electronic part of the bright A_W exciton at a delay of around 0 fs and 1.7 eV above the valence-band maximum (orange dashed line; exciton density (5.4 ± 1.0) × 10^{12} cm^{-2}; compare with Extended Data Fig. 8b)[26–28,34]. On the few-hundred-femtosecond timescale, we observe the formation of a second peak at lower photoemission energy (red dashed line). We identify this peak as the photoemitted electronic contribution of the ILX. The long-lived photoemission signature is detected below the A_W exciton resonance at about 1.1 eV above the valence-band maximum of WSe_2, in agreement with static photoluminescence experiments on a WSe_2/MoS_2 heterobilayer[35]. For the unambiguous attribution of the photoemission yield to an interlayer effect, we repeated the same analysis with data obtained from monolayer WSe_2 (Fig. 2b and dashed orange circle in Fig. 1c). Here, no spectral weight is observed in the ILX's energetic region, which clearly shows that the spectral weight in the heterobilayer measurement results from the charge transfer of the electron contribution of the exciton into the MoS_2 layer. We note that the identification of the ILX is in agreement with a recent trARPES study on 2°-twisted WSe_2/MoS_2 (ref. [13]). Interestingly, in addition to the electron contribution to the ILX, ref. [13] also identified the hole contribution to the ILX in energy–momentum-resolved spectra. Such a signature is not found in our analysis (Fig. 1b), which is most likely related to the different twist angles and related exciton confinement effects.

The exact mechanism of the ILX formation and the corresponding ultrafast charge separation is still a major open question[20]. It has been proposed that the ILX can be formed through interlayer tunnelling of its electron contribution at the K valleys[5,6], or, alternatively, through the intermediate formation of dark intralayer excitons, where the electron contribution is first scattered to the Σ valley and, subsequently, transferred to the neighbouring layer[4,36,37]. In this context, the strength of the trARPES experiment is that the femtosecond evolution of optically dark Σ_W excitons can be explicitly monitored[26–28]. In Fig. 2c, we therefore investigate the delay-dependent transfer of spectral weight between the electronic parts of the bright WSe_2 A_W exciton, the dark WSe_2 Σ_W

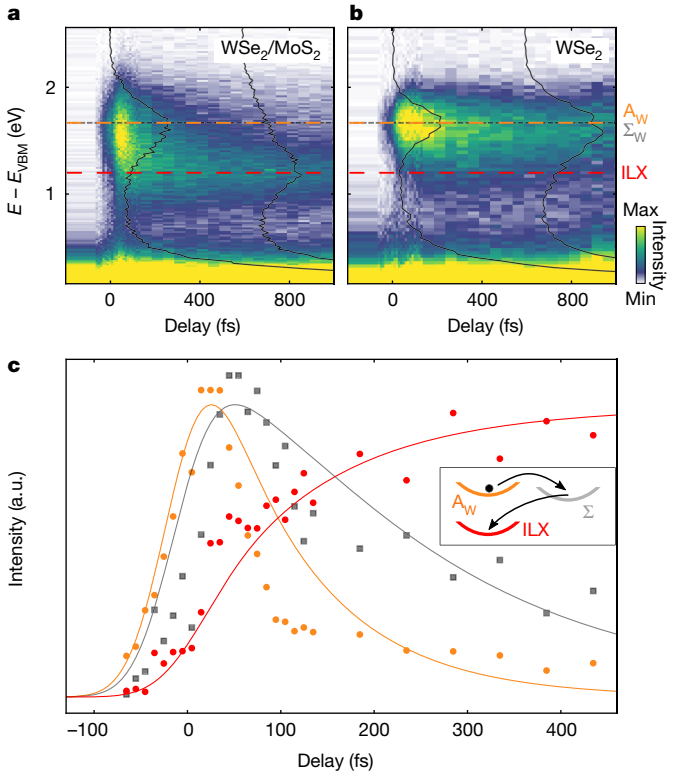

Fig. 2 | Ultrafast formation dynamics of ILXs. a,**b**, Delay-dependent evolution of the momentum-integrated energy-distribution curves for WSe_2/MoS_2 (**a**) and WSe_2 (**b**). In the monolayer, the signal decays on the picosecond timescale without a notable change in binding energy (dashed orange and grey lines). In the heterobilayer, the ILX formation is evident by the shift of spectral weight to smaller binding energies on the sub-100-fs timescale (dashed red line). The black line profiles are exemplary energy-distribution curves taken at −5 fs and 585 fs. **c**, The ILX formation is extracted through the delay-dependent photoemission yield of the ILX (red), the bright A_W excitons (orange) and the dark Σ_W excitons (grey; details on data analysis in Extended Data Figs. 6 and 7). The data points are experimental data and solid lines are calculated within a fully microscopic model. The inset shows the dominant charge-transfer channel. The energy-distribution curves in **a** and **b** are corrected for space-charge- and photovoltage-induced rigid band shifts of maximally 70 meV (Extended Data Fig. 8a).

exciton and the ILX (data handling in Extended Data Figs. 6 and 7; long-term picosecond dynamics in Extended Data Fig. 9). Initially, during the duration of the pump pulse, we find that bright WSe_2 A_W excitons are efficiently excited (orange data points). Subsequently, the weight of their photoemission signature decreases in intensity, whereas, concomitant, spectral yield is detected for the WSe_2 Σ_W exciton (grey) and the ILX (red). In particular, we find that for the time evolution after the optical excitation and the initial build-up, the decrease of spectral weight of the electronic contribution of the Σ_W exciton is synchronous to the increase of spectral weight of the ILX, strongly hinting at an ILX formation process through intermediate scattering through the Σ_W valley. Here, a quantitative analysis yields delayed onsets with respect to the A_W-exciton signal of 33 ± 6 fs for the Σ_W-exciton formation and 54 ± 7 fs for the ILX (Extended Data Fig. 9a). To corroborate the proposition of interlayer charge transfer through the Σ_W valley, we compare the trARPES data with predictions stemming from a fully microscopic model. We combine the density matrix formalism[6,38] with material-specific parameters from first principle calculations to simulate the formation dynamics of interlayer excitons after the optical excitation of intralayer excitons. In the model, we include the full exciton landscape of bright and dark intralayer, interlayer and hybrid excitons and all phonon-assisted transition channels between these states. We find that the most efficient exciton relaxation pathway is given by the cascade of optically excited exciton states $A_W \rightarrow \Sigma_W \rightarrow$ ILX (inset in Fig. 2c; compare with Supplementary Information). The direct comparison of experiment (symbols) and theory (lines) in Fig. 2c confirms an excellent agreement. This shows, from both an experimental and a theoretical point of view, that phonon-assisted scattering through dark-layer mixed states is indeed the dominant pathway for the formation of the ILX in the 9.8 ± 0.8°-twisted WSe_2/MoS_2 heterostructure.

The ILX moiré superlattice hallmark

Although trARPES with XUV pulses is an ideal approach to study the ILX formation process, the combination with multidimensional momentum microscopy allows the identification of momentum-space signatures that are caused by the real-space moiré superlattice. In this manner, Fig. 3a–c shows the momentum structure of the A_W exciton, the Σ_W exciton and the ILX, respectively (additional data in Extended Data Fig. 6). Although the momentum fingerprints of the A_W exciton and the Σ_W exciton appear as expected[26,27], the ILX momentum structure is clearly more complex. Without consideration of the moiré superlattice, for the ILX, one would expect to detect photoemission yield at the in-plane momentum of the electron contribution to the quasiparticle, that is, at the K_{Mo} (K'_{Mo}) valleys of MoS_2 (corners of the dotted dark red hexagon in Fig. 3c). However, the measured momentum fingerprint shows a strikingly richer structure. We observe a complex momentum structure that is dominated by three peaks that are centred around the K_W (K'_W) valleys (orange hexagon in Fig. 3c). Apparently, the ILX momentum fingerprint exhibits additional features that are not observed for any other spectral feature in our data: so far, all other occupied bands and excitonic states were unambiguously assignable to the periodicity of either the WSe_2 top layer or the MoS_2 bottom layer.

The most interesting question now is whether the observed ILX momentum structure may be identified as a hallmark of the moiré superlattice that is created by the 9.8 ± 0.8°-twisted Brillouin zones of WSe_2 and MoS_2. To answer this question, we construct the momentum-space equivalent of the real-space moiré periodicity, which is the mini Brillouin zone (mBZ) that is shown on top of the momentum-resolved photoemission data of the ILX in Fig. 3c (red hexagon). Within the mBZ, we can now unambiguously identify that the three-peak structure is indeed a fingerprint of the moiré superlattice, as the spectral features clearly coincide with the high-symmetry κ valleys of the mBZ.

Having identified the correlation between the ILX momentum fingerprint and the moiré superlattice, we aim to model the distinct photoemission intensity distribution of the ILX. For this purpose, we make use of previous studies on interlayer interaction in incommensurate atomic layers[39]. In particular, we follow the notation in ref. [39], where the interlayer coupling in reciprocal space is expressed in terms of a generalized umklapp process (Fig. 3d; details in Methods). A straightforward geometrical construction following this work yields the intensity distribution shown in Fig. 3d: the highest photoemission yield is expected for momenta marked by circles, which correspond to the κ points of the mBZ. Weaker photoemission yield is expected in areas marked by squares, which indeed are partially and faintly visible in the data. Finally, negligible signal is expected in momentum areas marked by triangles, consistent with our experimental data.

However, despite the good agreement of the data with this generalized umklapp process, the interpretation of the momentum structure being a result of interlayer interaction is not obvious, because interlayer coupling at the K valleys was mostly regarded as negligibly small owing to the in-plane orbital character in this valley[4,36]. A regular final-state scattering can be excluded, as only the ILX signal is exhibiting these replicas. The threefold signal should also not be a result of an exciton wavefunction that is confined in a single moiré potential well, as a modification of the

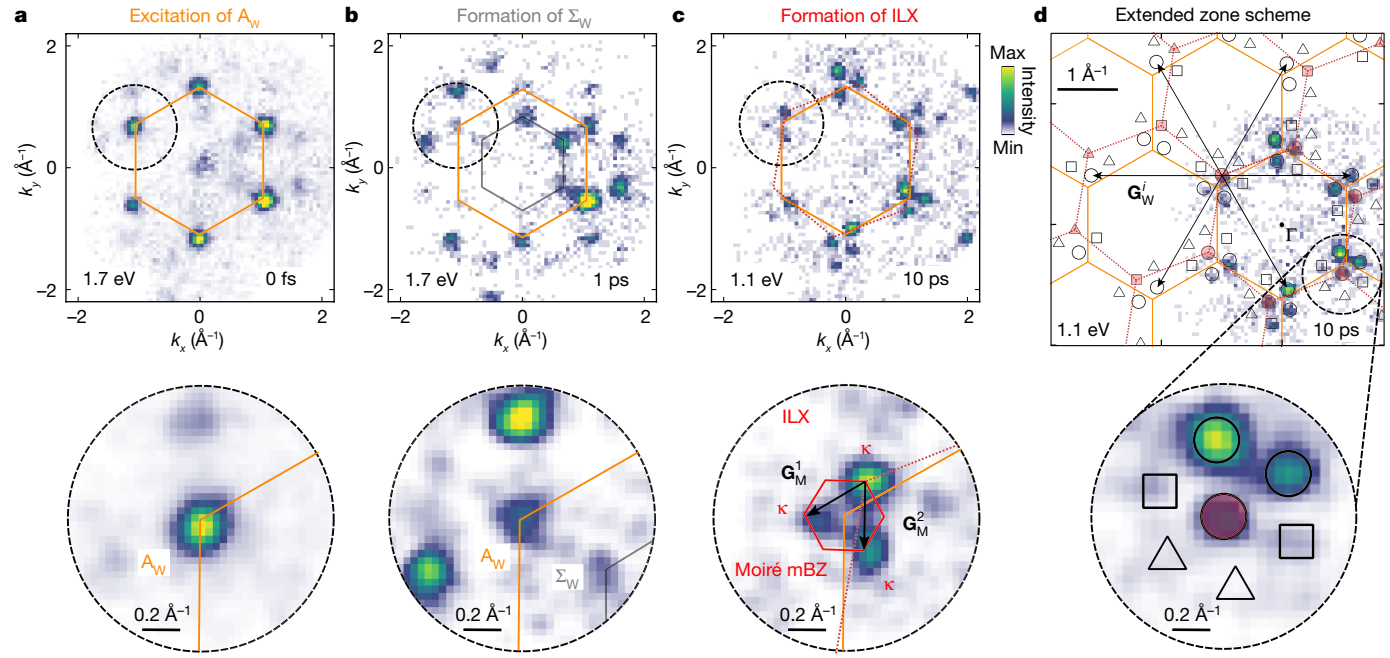

Fig. 3 | Momentum fingerprints of the moiré interlayer excitons. **a**–**c**, Momentum fingerprints of the bright A_W exciton (**a**), the dark Σ_W exciton (**b**) and the ILX (**c**). Photoemission yield of the A_W exciton, the Σ_W exciton, and the ILX are detected at the K_W valleys (orange hexagon), the Σ_W valleys (black hexagon) and the κ valleys of the mBZ (red hexagon), respectively. The bottom row shows zoom-ins from the circled areas in the top row. **d**, The intensity distribution of the momentum fingerprint of the ILX can be constructed using a generalized umklapp process[39]. The red filled symbols label K_{Mo} valleys of the first (circles) and higher-order (squares and triangles) Brillouin zones. Open circles, squares and triangles represent a hierarchy of expected spectral weight from high to low, resulting from generalized umklapp processes with WSe_2 reciprocal lattice vectors $\mathbf{G}^i_W$ (black arrows).

relative or centre-of-mass motion of the electron–hole pair becomes important for only large moiré wavelengths, that is, for twist angles less than 2° (refs. [10–12]), in agreement with a recent momentum microscopy experiment[13] (Extended Data Fig. 10). Instead, as the photoemitted electron of the ILX has been bound to a hole that remains in the heterostructure, we find here that the umklapp process is transferred through the Coulomb interaction. Thus, to imprint the moiré superlattice onto the excitonic photoemission signal, it is necessary that the electron and the hole components are found in the neighbouring TMD layers such that the quasiparticle experiences the lattice periodicities of both. In consequence, for intralayer A_W and Σ_W excitons, where electron and hole reside in WSe_2, we do not expect and also do not observe the moiré superlattice hallmark in the momentum-resolved photoemission intensity (Fig. 3a,b and Extended Data Fig. 4). To unambiguously assign the microscopic origin of the moiré hallmark in the excitonic momentum fingerprint, however, further theory on photoemission from excitonic quasiparticles is necessary. Nevertheless, our analysis shows that the complex momentum structure of the ILX is a hallmark fingerprint of moiré superlattice modification that has not been observed so far and is clearly unique for the ILXs in a twisted heterostructure.

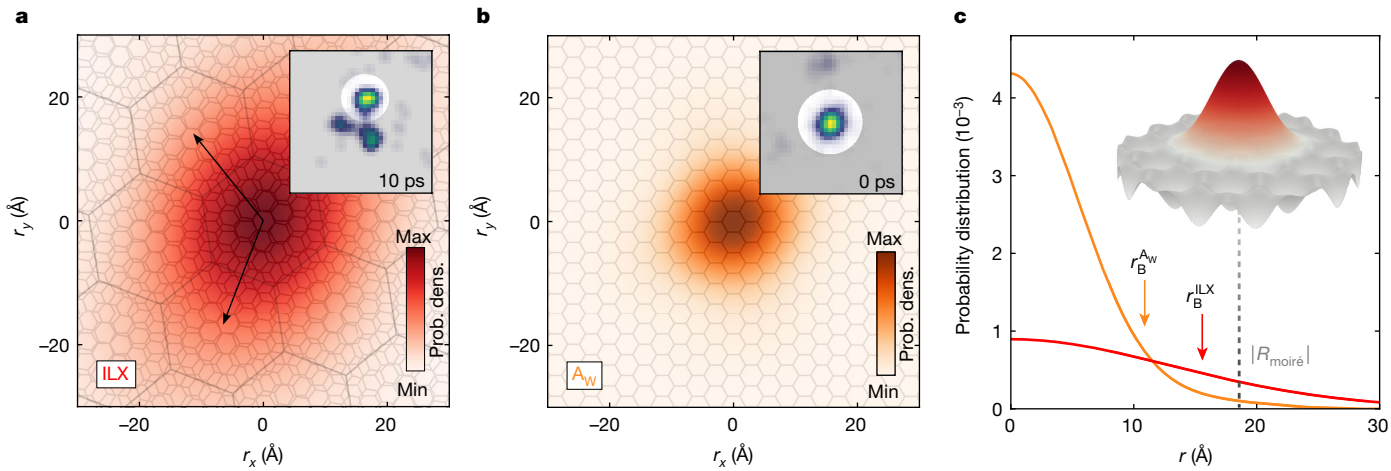

Fig. 4 | Real-space exciton wavefunction reconstruction and spatial relation to the moiré superlattice. **a**,**b**, Real-space reconstructions of the wavefunction of the electron contribution to the ILX (**a**) and the WSe_2 A_W exciton (**b**). In **a**, the overlay with small (atomic lattices of the twisted WSe_2 and MoS_2 layers) and large (moiré lattice) hexagons illustrates the extension of the electron contribution to the ILX wavefunction over multiple moiré unit cells (black arrows, moiré lattice vectors). In **b**, only the lattice periodicity of WSe_2 is overlain on the data. The insets show the masks used to select a single valley for the reconstruction. **c**, Line profiles through the probability density. The inset schematically shows how the electronic contribution to the ILX wavefunction (red) is spread over multiple moiré cells (grey).

ILX real-space wavefunction analysis

Finally, we determine the electron contribution to the real-space wavefunction of intra- and interlayer excitons. We follow the framework of photoemission orbital tomography[40] and recent developments that have been carried out for TMD excitons[13,28,34]. We use the relation $I(k_x, k_y) \propto |\mathrm{FT}\{\Psi(r_x, r_y)\}|^2$ that connects the real-space wavefunction $\Psi(r_x, r_y)$ with the momentum-resolved photoemission intensity $I(k_x, k_y)$ within the plane-wave approximation[28,40] (Methods). The multidimensional data collection scheme now facilitates the direct comparison of the real-space extension $r_{x,y}$ of the electronic wavefunction contribution of the excitons with the spatial extension of the moiré unit cell (Fig. 4). We extract the respective Bohr radii as $r_B^{ILX} = 1.6 \pm 0.2$ nm and $r_B^{A_W} = 1.1 \pm 0.1$ nm (root mean square), which is in agreement with a recent analysis[13] (Methods). We can draw two conclusions. The extension of the electronic contribution to the ILX wavefunction is larger than the moiré period of the 9.8 ± 0.8°-twisted heterostructure ($|R_{moiré}| = 1.84 \pm 0.15$ nm), that is, the ILX can propagate laterally through the heterostructure and is not confined to a single moiré potential well. Second, the analysis shows that the ILX extension is significantly broader than that of the WSe_2 A_W exciton. The charge separation across the two TMD layers leads to a weaker attractive interaction between the electron and the hole contribution to the exciton, and the wavefunction exhibits a larger spread in real space.

Online content

Any methods, additional references, Nature Research reporting summaries, source data, extended data, supplementary information, acknowledgements, peer review information; details of author contributions and competing interests; and statements of data and code availability are available at https://doi.org/10.1038/s41586-022-04977-7.

1. Hong, X. et al. Ultrafast charge transfer in atomically thin MoS_2/WS_2 heterostructures. *Nat. Nanotechnol.* **9**, 682–686 (2014).
2. Rivera, P. et al. Observation of long-lived interlayer excitons in monolayer $MoSe_2$–WSe_2 heterostructures. *Nat. Commun.* **6**, 6242 (2015).
3. Kim, J. et al. Observation of ultralong valley lifetime in WSe_2/MoS_2 heterostructures. *Sci. Adv.* **3**, e1700518 (2017).
4. Wang, Y., Wang, Z., Yao, W., Liu, G.-B. & Yu, H. Interlayer coupling in commensurate and incommensurate bilayer structures of transition-metal dichalcogenides. *Phys. Rev. B* **95**, 115429 (2017).
5. Merkl, P. et al. Ultrafast transition between exciton phases in van der Waals heterostructures. *Nat. Mater.* **18**, 691–696 (2019).
6. Ovesen, S. et al. Interlayer exciton dynamics in van der Waals heterostructures. *Commun. Phys.* **2**, 23 (2019).
7. Förg, M. et al. Moiré excitons in $MoSe_2$–WSe_2 heterobilayers and heterotrilayers. *Nat. Commun.* **12**, 1656 (2021).
8. Yu, H., Liu, G.-B., Tang, J., Xu, X. & Yao, W. Moiré excitons: from programmable quantum emitter arrays to spin–orbit-coupled artificial lattices. *Sci. Adv.* **3**, e1701696 (2017).
9. Wu, F., Lovorn, T. & MacDonald, A. H. Theory of optical absorption by interlayer excitons in transition metal dichalcogenide heterobilayers. *Phys. Rev. B* **97**, 035306 (2018).
10. Seyler, K. L. et al. Signatures of moiré-trapped valley excitons in $MoSe_2$/Wse_2 heterobilayers. *Nature* **567**, 66–70 (2019).
11. Alexeev, E. M. et al. Resonantly hybridized excitons in moiré superlattices in van der Waals heterostructures. *Nature* **567**, 81–86 (2019).
12. Tran, K. et al. Evidence for moiré excitons in van der Waals heterostructures. *Nature* **567**, 71–75 (2019).
13. Karni, O. et al. Structure of the moiré exciton captured by imaging its electron and hole. *Nature* **603**, 247–252 (2022).
14. Su, J.-J. & MacDonald, A. H. How to make a bilayer exciton condensate flow. *Nat. Phys.* **4**, 799–802 (2008).
15. Wu, F., Lovorn, T., Tutuc, E. & MacDonald, A. H. Hubbard model physics in transition metal dichalcogenide moiré bands. *Phys. Rev. Lett.* **121**, 026402 (2018).
16. Cao, Y. et al. Unconventional superconductivity in magic-angle graphene superlattices. *Nature* **556**, 43–50 (2018).
17. Wang, L. et al. Correlated electronic phases in twisted bilayer transition metal dichalcogenides. *Nat. Mater.* **19**, 861–866 (2020).
18. Regan, E. C. et al. Mott and generalized Wigner crystal states in WSe_2/WS_2 moiré superlattices. *Nature* **579**, 359–363 (2020).
19. Rivera, P. et al. Interlayer valley excitons in heterobilayers of transition metal dichalcogenides. *Nat. Nanotechnol.* **13**, 1004–1015 (2018).
20. Jin, C. et al. Ultrafast dynamics in van der Waals heterostructures. *Nat. Nanotechnol.* **13**, 994–1003 (2018).
21. Novoselov, K. S. et al. A roadmap for graphene. *Nature* **490**, 192–200 (2012).
22. Wang, G. et al. Colloquium: Excitons in atomically thin transition metal dichalcogenides. *Rev. Mod. Phys.* **90**, 021001 (2018).
23. Mueller, T. & Malic, E. Exciton physics and device application of two-dimensional transition metal dichalcogenide semiconductors. *npj 2D Mater. Appl.* **2**, 29 (2018).
24. Geim, A. K. & Grigorieva, I. V. Van der Waals heterostructures. *Nature* **499**, 419–425 (2013).
25. Yu, H., Wang, Y., Tong, Q., Xu, X. & Yao, W. Anomalous light cones and valley optical selection rules of interlayer excitons in twisted heterobilayers. *Phys. Rev. Lett.* **115**, 187002 (2015).
26. Madéo, J. et al. Directly visualizing the momentum-forbidden dark excitons and their dynamics in atomically thin semiconductors. *Science* **370**, 1199–1204 (2020).
27. Wallauer, R. et al. Momentum-resolved observation of exciton formation dynamics in monolayer WS_2. *Nano Lett.* **21**, 5867–5873 (2021).
28. Dong, S. et al. Direct measurement of key exciton properties: energy, dynamics, and spatial distribution of the wave function. *Nat. Sci.* **1**, e10010 (2021).
29. Taniguchi, T. & Watanabe, K. Synthesis of high-purity boron nitride single crystals under high pressure by using Ba–BN solvent. *J. Cryst. Growth* **303**, 525–529 (2007).
30. Medjanik, K. et al. Direct 3D mapping of the Fermi surface and Fermi velocity. *Nat. Mater.* **16**, 615–621 (2017).
31. Keunecke, M. et al. Time-resolved momentum microscopy with a 1 MHz high-harmonic extreme ultraviolet beamline. *Rev. Sci. Instrum.* **91**, 063905 (2020).
32. Keunecke, M. et al. Electromagnetic dressing of the electron energy spectrum of Au(111) at high momenta. *Phys. Rev. B* **102**, 161403 (2020).
33. Wilson, N. R. et al. Determination of band offsets, hybridization, and exciton binding in 2D semiconductor heterostructures. *Sci. Adv.* **3**, e1601832 (2017).
34. Man, M. K. L. et al. Experimental measurement of the intrinsic excitonic wave function. *Sci. Adv.* **7**, eabg0192 (2021).
35. Karni, O. et al. Infrared interlayer exciton emission in MoS_2/WSe_2 heterostructures. *Phys. Rev. Lett.* **123**, 247402 (2019).
36. Kunstmann, J. et al. Momentum-space indirect interlayer excitons in transition-metal dichalcogenide van der Waals heterostructures. *Nat. Phys.* **14**, 801–805 (2018).
37. Wallauer, R. et al. Momentum-resolved observation of ultrafast interlayer charge transfer between the topmost layers of MoS_2. *Phys. Rev. B* **102**, 125417 (2020).
38. Brem, S., Linderälv, C., Erhart, P. & Malic, E. Tunable phases of moiré excitons in van der Waals heterostructures. *Nano Lett.* **20**, 8534–8540 (2020).
39. Koshino, M. Interlayer interaction in general incommensurate atomic layers. *New J. Phys.* **17**, 015014 (2015).
40. Puschnig, P. et al. Reconstruction of molecular orbital densities from photoemission data. *Science* **326**, 702–706 (2009).

Methods

Heterostructure fabrication

The WSe_2/MoS_2/hexagonal boron nitride (hBN) heterostructures were assembled using mechanical exfoliation and dry transfer, as summarized in Extended Data Fig. 1a–d. First, a p^+-silicon (Si) substrate (1–10 Ωcm) with polished native oxide was plasma cleaned with oxygen gas (100 W, 10 standard cubic centimetres per minute, 10 min). hBN was immediately mechanically exfoliated on the substrate using standard office tape. Using optical contrast, a hBN flake with thickness between 20 nm and 30 nm was identified. In parallel, MoS_2 and WSe_2 (HQ graphene) were mechanically exfoliated using blue tape (Ultron Systems 1008R-6.0) on a polydimethylsiloxane (PDMS) sheet (Gel-Pak PF-20/17-X4). Similar to hBN exfoliation, optical contrast was used to identify monolayer MoS_2 and WSe_2. Unlike the standard dry-transfer assembly, the assembly of the heterostructure was started by assembling the WSe_2/MoS_2 heterostructure on PDMS first. The two flakes were aligned visually and the MoS_2 flake was dry transferred on top of the WSe_2 flake on PDMS. Then the WSe_2/MoS_2 heterostructure was dry transferred on top of the hBN. During the last transfer, the multilayer part of the WSe_2 flake was intentionally placed in direct contact with the Si substrate to reduce sample charging (compare with Extended Data Fig. 1e,f). It is worth noting that although the exfoliation part was done in ambient conditions, the heterostructure assembly was done in a controlled argon environment in a glovebox with oxygen and water <0.1 ppm. An optical microscope image of the van der Waals stack is shown in Extended Data Fig. 1e.

Sample preparation for photoemission spectroscopy

The Si wafer with the heterostructure is clamped onto a sample holder under ambient conditions and transferred into ultrahigh vacuum. In an ultrahigh-vacuum preparation chamber (background pressure $<5 \times 10^{-9}$ mbar), the sample is annealed for 2 h at a temperature of approximately 670 K; such sample treatment has shown successful ARPES results on similar sample systems, for example, ref. [41]. Subsequently, the sample is transferred into the momentum microscope. All experiments have been performed at room temperature at a background pressure of approximately 1×10^{-10} mbar.

Femtosecond momentum microscopy

The experimental set-up is detailed and benchmarked in ref. [31]. It consists of two major parts, namely, a time-of-flight momentum microscope[30] (ToF Momentum Microscope , Surface Concept), shown schematically in Fig. 1a, and a high-power femtosecond laser system (Active Fiber Systems). In the following, we briefly describe the experimental set-up.

The strength of the time-of-flight momentum microscope is the simultaneous measurement of the two-dimensional in-plane momenta and the kinetic energy of the photoelectrons within the full photoemission horizon[30]. To study high-quality TMD heterostructures with a diameter of approximately 10 μm, the key advantage of the set-up lies in the microscopy-type photoelectron detection scheme. In the electrostatic lens system, a real- and a reciprocal-space image of the photoelectrons is formed and either image can be projected onto the photoelectron detector (Fig. 1a). The real-space mode of the microscope is used to map the spatial structure of the sample system (Fig. 1c and Extended Data Fig. 1f). In direct comparison with an optical microscope image (Extended Data Fig. 1e), the monolayer WSe_2 and MoS_2 regions as well as the WSe_2/MoS_2 heterobilayer region can be identified through the differing photoemission contrast. By placing an aperture into the real-space plane of the microscope, either photoelectrons originating from the WSe_2 monolayer or the WSe_2/MoS_2 heterobilayer can be selected and projected onto the detector (Extended Data Fig. 2). By exploiting this capability of the time-of-flight momentum microscope, we collect in-plane momentum- and energy-resolved photoelectron distributions for the regions of interest highlighted by circles in Fig. 1c. The energy resolution of the momentum microscope combined with the spectral width of the 26.5-eV XUV light pulses lead to an overall Gaussian broadening of the measured photoelectron signal with a full-width at half-maximum of 200 ± 30 meV (ref. [31]). The achievable momentum resolution of the instrument is <0.01 $Å^{-1}$ (ref. [42]). From a fit of the cut-off of the photoemission horizon, we can verify that the momentum resolution for the given experimental settings in the paper is better than 0.04 ± 0.01 $Å^{-1}$. The time resolution is 54 ± 7 fs for infrared pump pulses of 50 ± 5 fs and XUV probe pulses of 21 ± 5 fs as used in this experiment[31]. This value is confirmed with a fit to the replica signal caused by the laser-assisted photoelectric effect (LAPE)[31,43] (see, for example, Fig. 3a or Extended Data Fig. 6c at 0-fs delay), which yields an infrared-pump–XUV-probe cross-correlation of 49 ± 1 fs.

The laser set-up is based on a 300-W fibre laser system (Active Fiber Systems) that operates at a repetition rate of 500 kHz and drives a high-harmonic generation beamline and a high-power optical parametric amplifier (OPA, Orpheus-F/HP from Light Conversion). To first induce and subsequently probe excitonic dynamics occurring in the TMD heterostructure (Fig. 2), we use a pump–probe scheme. First, bright WSe_2 A_W excitons are excited with light pulses generated with the OPA (1.7 eV, 50 ± 5 fs measured per autocorrelation). Subsequently, the femto- to picosecond evolution of the intra- and interlayer excitonic dynamics is probed with an XUV light pulse (26.5 eV, *p*-polarized, 21 ± 5 fs (ref. [31])), which photoemits the electron contribution of the quasiparticle into the detector. Additional experiments are performed with 1.9-eV and 2.4-eV pump light, which is generated through the OPA and frequency doubling of the compressed laser output, respectively. The data in Figs. 1b and 2, and Extended Data Figs. 4c,d, 5, 7, 8a,b and 9 are obtained with an *s*-polarized pump light. The data in Figs. 3 and 4, and Extended Data Figs. 4a,b and 6 are obtained with a *p*-polarized pump light. For the *p*-polarized pump, one creates band replicas owing to the LAPE, which then can be used to determine pump– probe overlap (time zero) and the time resolution[32,43]. For the *s*-polarized pump, the time-resolved signal is free of such LAPE replicas, which is helpful for the analysis of spectral features and exciton dynamics.

Real-space imaging and static band mapping of WSe_2/MoS_2/hBN

After preparation of the van der Waals stack for the momentum microscopy experiment, we first perform real-space imaging of the sample with an ultraviolet diode delivering 4.96-eV photons. In Extended Data Fig. 1e,f, the photoemission real-space map is compared with an optical microscope image. In both images, the WSe_2/MoS_2/hBN heterostructure, the doped Si substrate, the bulk hBN, the WSe_2 and MoS_2 monolayers, and the bulk WSe_2 can be distinguished.

Having identified the regions of interested, we place an aperture into the real-space image of the microscope to selectively probe the energy- and momentum-resolved photoelectron distribution of the WSe_2 monolayer and the WSe_2/MoS_2 heterobilayer (compare with Fig. 1a). Using an aperture with a diameter of 100 μm and a lens setting with a magnification of 10, we are sensitive to photoelectrons originating from an effective area with diameter of 10 μm on the heterostructure (circles in Fig. 1c).

Static band mapping of the occupied electronic band structure is shown in Extended Data Fig. 2. The high quality of the van der Waals stack is evident from the well resolved features in the band structure and, in particular, by the visible spin-splitting of the WSe_2 valence bands at the K_W and K'_W valleys[44] (marked with 1 and 2 in Extended Data Fig. 2). In addition, only in the heterobilayer region, we resolve clear signatures of the valence-band maximum of MoS_2 at −1.1 eV with respect to the valence-band maximum (E_{VBM}) of WSe_2 (marked with 3 in Extended Data Fig. 2b). Owing to interlayer interaction between the WSe_2 and MoS_2 layers, we resolve the expected hybridized valence bands at the $\Gamma_{W,Mo}$ valley (marked with 4 and 5 in Extended Data Fig. 2b)[33]. The observation of these hybridized bands is a clear signature that the blisters found in

the real-space image in Extended Data Fig. 1e,f do not dominate the photoemission yield from the heterobilayer. In contrast, in the monolayer WSe_2 region, the valence band at the Γ_W valley is a single band (Extended Data Fig. 2a). Furthermore, the valence-band maximum is localized at the K_W (K'_W) valley, as expected for the monolayer limit of WSe_2, where it becomes a direct bandgap semiconductor[33]. In addition, we observe a clear signature of the valence band of hBN that we label with 6 in Extended Data Fig. 2a. Within our energy and momentum resolution, we do not resolve moiré induced mini-band replicas of the valence bands, such as discussed in refs. [41,45].

Inhomogeneous broadening from sample

In our experiment, the energy resolution is mainly limited by the bandwidth of the short-pulse XUV light source. Convolved with the instrument resolution, we achieve a total energy resolution on the order of 200 ± 30 meV (ref. [31]). For reference, Extended Data Fig. 3 shows an exemplary energy-distribution curve obtained in a momentum region of ±0.10 $Å^{-1}$ centred at the K'_W valley. As in the case of ref. [26], we extract a full-width at half-maximum of 280 ± 10 meV. However, our spectrum is broadened by 200 meV by the light source and the instrument, so that the full-width at half-maximum peak width of the valence-band maximum is on the order of 200 meV. This broadening is attributed to, for example, inhomogeneity of the sample and local field effects.

Twist-angle determination of the WSe_2/MoS_2 heterostack

In trARPES experiments, it is known that the electron contribution of the A excitons are identified through spectral weight at the corresponding K valleys of the TMD structure[26–28]. Consequently, the photoemission signature of the A_W and A_{Mo} excitons can directly be used to determine the twist angle of a heterostructure. Here, for the unambiguous identification of the A_W and A_{Mo} excitons in the K_W and K_{Mo} valleys, we carry out resonant excitation using 1.7-eV and 1.9-eV pump light, respectively.

In Extended Data Fig. 4, we show momentum maps of the resonantly pumped WSe_2 A_W exciton (Extended Data Fig. 4a), the resonantly pumped MoS_2 A_{Mo} exciton (Extended Data Fig. 4c), and the corresponding signature of the ILX after a delay of 1 ps (Extended Data Fig. 4b,d). From the misalignment of the Γ–K_W and Γ–K_{Mo} directions (orange and dark red dashed lines), we calculate the momentum mismatch between the K_W and the K_{Mo} valleys, and, accordingly, determine the twist angle to $\Theta = 9.8 \pm 0.8°$. The direct comparison with the 1-ps data in Extended Data Fig. 4b,d then facilitates the correlation of the ILX momentum signature to the in-plane momenta of the K_W and the K_{Mo} valleys.

Spectral assignments of conduction and valence bands and the $A_{W,Mo}$ excitons

We study the ultrafast exciton dynamics of the heterobilayer after resonant excitation of the A_W exciton of WSe_2 with 1.7-eV pump pulses. To unambiguously identify the photoemission signatures shown in Figs. 2 and 3 as excitons, Extended Data Fig. 5a,b shows energy–momentum cuts when using above-bandgap excitation conditions with 2.4-eV pump pulses to the monolayer WSe_2 region indicated by the orange circle in Fig. 1c. In temporal overlap of the pump and probe laser pulses (0 fs), above-bandgap excitation allows for the transient occupation of the conduction band and we correspondingly observe parabolic bands with positive dispersion centred at $E - E_{VBM} = 1.8$ eV at the K_W valley. As the delay is increased to 300 fs, the spectral yield at the K_W valley shifts to smaller energies and the parabolic signature transfers to a more spherical shape. We attribute the photoemission yield from the parabolic dispersion at 0 fs to photoelectrons originating from both higher-quantum-number excitons and charge carriers from the conduction band of WSe_2, as has been described previously and is in full agreement with ref. [26]. Subsequently, the delay-dependent shift of the spectral weight to smaller energies can be understood by the formation of excitons (compare with the energy-distribution curves in Extended Data Fig. 5b). In Extended Data Fig. 5c, we compare the above-bandgap excitation results with energy-distribution curves obtained from the 1.7-eV pump-light experiment. Under these resonant excitation conditions, already at 0-fs pump–probe delay the exciton signal is observed at $E - E_{VBM} = 1.7$ eV. Importantly, the signal does not decrease in energy with proceeding delay and does not show a positive parabolic dispersion (compare with Fig. 1b and Extended Data Fig. 6).

By repeating the same analysis as described above for a monolayer MoS_2 sample, we can discriminate the A_{Mo} exciton from charge carriers in the conduction-band minimum (Extended Data Fig. 5d–f). It is noted that we do not resolve the pump–probe delay-dependent energy shift for the case of MoS_2, but the parabolic momentum dispersion at 0 fs can again be distinguished from the more spherical shape at 250 fs.

Additional time-resolved momentum microscopy data of the twisted WSe_2/MoS_2 heterostructure

Extended Data Fig. 6 summarizes, in addition to Fig. 3, $E(k)$ and k_x–k_y momentum maps of the formation dynamics of the ILX.

Filtering excitonic photoemission signatures in energy and momentum space

The time-of-flight momentum microscope collects in-plane momentum and energy-resolved data cubes for each pump–probe delay[31]. To monitor the pump–probe delay-dependent exciton dynamics, the excitonic photoemission signatures need to be filtered on these coordinates to avoid mixing of different photoemission signals. Therefore, in Extended Data Fig. 7a,b, we show two momentum maps that are integrated for all measured pump–probe delays in an energy window between $E - E_{VBM} = 1.5$–2.4 eV and $E - E_{VBM} = 0.8$–1.3 eV, respectively. First, we recognize that the signal of the Σ_W exciton (black circle) can be easily separated from the A_W exciton (orange) and the ILX (red) in momentum space. Still, we choose the lower bound of the integration window for the Σ_W-exciton signal well above the energy of the ILX on the energy axis to determine the pump–probe-delay-dependent spectral weight plotted in Fig. 2c (integration window $E - E_{VBM} = 1.5$–2.4 eV). The separation of the spectral weight of the A_W exciton and the ILX needs to be further analysed and filtered on the energy axis as, in momentum space, the regions of interest are close to each other. From the evolution of the energy-distribution curves of the A_W-exciton-momentum-filtered areas in Extended Data Fig. 7c (upper panel), it is obvious that the A_W photoemission signal strongly dominates over the ILX signal for $E - E_{VBM} > 1.5$ eV. Consequently, in Fig. 2c, we plot the A_W-exciton signal as obtained within the momentum region indicated by the orange circles in Extended Data Fig. 7a and for $E - E_{VBM} = 1.5$–2.4 eV (orange boxed energy region in Extended Data Fig. 7c, upper panel). For the ILX signal, the correct identification of the energy-integration window is more complex and therefore further analysed based on the evolution of the energy-distribution curves of the ILX-momentum-filtered areas in Extended Data Fig. 7c (middle panel). To separate the signal of the ILX, which is centred at $E - E_{VBM} \approx 1.1$ eV, from the photoemission yield at higher energies, we systematically vary the energy window that is used to integrate the ILX signal (blueish boxes in Extended Data Fig. 7c, middle panel). The resulting spectral weight versus pump–probe delay plots are shown in the lower panel of Extended Data Fig. 7c. For small-energy-integration boxes (dark blue and blue), we find an identical evolution of the spectral weight that we attribute to the ILXs. However, as the box becomes too large (light blue), at about 50 fs, spurious signal from higher energies leads to deviations. Consequently, we use the appearance of this additional photoemission signal at about 50 fs to determine the upper bound of the maximum energy-integration window for the ILXs to $E - E_{VBM} < 1.3$ eV. This sets the boundaries for the energy-integration box of the ILXs to $E - E_{VBM} = 0.8$–1.3 eV, which is plotted in Fig. 2c.

Correction of space-charge and photovoltage effects

In trARPES experiments, even in the sub-1 mJ cm^{-2} fluence regime, one often observes space-charge and/or photovoltage effects. These effects are induced by Coulomb interaction of the photoelectrons or the remaining holes, which were excited by the pump and the probe laser pulses[46–48]. These effects are well known in the trARPES community and, in a moderate regime, cause only a rigid spectral shift of all probe photoelectrons, that is, a shift of the entire photoelectron spectrum. In this regime, one automatically monitors space-charge- and photovoltage-induced shifts when collecting the trARPES data and one correspondingly corrects for these 'rigid' shifts before analysing the data. For all data presented in our paper, we observe such rigid shifts of the full ARPES spectrum, which is on the order of several millielectronvolts up to a maximum of about 70 meV (Extended Data Fig. 8a). The pump–probe-delay-dependent energy difference ΔE is calculated by fitting a selected peak in the full momentum-integrated energy-distribution curves and subtracting its energy position from the reference measurement data shown in the inset. Although this energy difference ΔE is small compared with our energy resolution and barely influences the analysis procedure, we routinely correct our data for these effects before carrying out the data analysis. This means that all data shown in this paper are corrected for this rigid energy offset. It is noted that for the analysis of the ILX momentum fingerprint, the energy shift is irrelevant, because the data are analysed on the picosecond timescale.

Determination of the exciton density

It has been shown in TMDs that for optical pumping with sufficiently high fluence, a Mott transition from excitonic states to free carriers can be induced when the excited exciton density is in the range of 10^{12}–10^{14} cm^{-2} (refs. [49–53]). This transition leads to giant bandgap renormalizations of up to 500 meV (ref. [49]) and thus might influence our interpretation of A_W-exciton generation and the subsequent dynamics. In the following, we describe the calculation of the exciton density in our experiment, and subsequently show pump–probe-delay-dependent energy-distribution curves of the valence-band maxima of WSe_2 to directly exclude the contribution of band renormalizations to our experimental analysis.

Using the real-space mode of the microscope, we can extract the $1/e^2$ radius of the pump beam on the sample to 151 ± 1 μm. For the data shown in Fig. 2c, the heterostructure was irradiated with *s*-polarized 1.7-eV photons with a peak fluence of 280 ± 20 μJ cm^{-2}. By following the analysis of ref. [50], we calculate the absorbed fluence to be 1.5 ± 0.2 μJ cm^{-2}, which results in an exciton density of (5.4 ± 1.0) × 10^{12} cm^{-2}. As this exciton density is in the 10^{12}–10^{14} cm^{-2} threshold regime[49–53], it is important to provide experimental evidence that our experiment probes excitons and not quasi-free carriers in the conduction bands.

We therefore analyse our data for the possible generation of quasi-free carriers and the corresponding renormalization of the band structure. In Extended Data Fig. 8b, we monitor the position of the WSe_2 valence-band maximum at the K_W valley compared with the position at −2 ps as a function of delay, which, in the case of generation of quasi-free carriers, is expected to strongly upshift in energy (compare with ref. [49]). In ref. [53], using trARPES, for example, the energetic position of the valence-band maximum shifts up by 360 meV and then relaxes back to its unperturbed value on the picosecond timescale. Importantly, within the scattering of our data (about ±50 meV in Extended Data Fig. 8b), the photoemission energy of the valence-band edge at the K_W valley does not change with pump–probe delay. In particular, it does not upshift in energy, as would be expected for an exciton density above the Mott threshold. This directly implies that the dominant excitation in our experiment is governed by A_W excitons in WSe_2, from which the subsequent exciton dynamics is induced, whereas the role of quasi-free carriers is negligible. It is noted that the error bars around 0 fs are enlarged because of a typical broadening of the occupied bands in temporal overlap (compare with Extended Data Fig. 6a,b).

Quantitative analysis of charge-transfer times to the Σ_W excitons and the ILX

The intermediate steps of the exciton dynamics occurring in the WSe_2/MoS_2 heterostructure are summarized in the excitation diagram shown in the inset of Fig. 2c. A_W excitons are resonantly excited with 1.7-eV pump photons, exciton–phonon scattering leads to the formation of Σ_W excitons and, subsequently, ILXs are formed through interlayer charge transfer at the Σ valleys. Typically, one would use a rate-equation model to quantify the respective charge-transfer times. However, this approach is not feasible here, as it does not accurately describe the coherent polarization induced when the pump pulse is present on the sample[27]. In addition, because of photoemission cross-section effects, we cannot unambiguously correlate the measured photoemission signal to the exciton occupation density, as would be necessary to extract meaningful transfer rates from a rate-equation model. Therefore, we assume the most simple model for a quantitative analysis. The states are filled by a Gaussian excitation or transfer rate. This rise in spectral weight follows an error function. In Extended Data Fig. 9a, we fit the pump–probe-delay-dependent spectral weight with error functions $I/I_{max} = 0.5 \times (\mathrm{erf}((t - t_i)/w) + 1)$, which give us access to the delayed onset $t_{\Sigma W}$ and t_{ILX} of the photoemission yield from the Σ_W exciton and the ILX, respectively, compared with the build-up of the A_W exciton (t_{AW}). We calculate delayed onset times of $t_{\Sigma W} - t_{AW} = 33 \pm 6$ fs and $t_{ILX} - t_{AW} = 54 \pm 7$ fs. These delayed onsets are in overall agreement with earlier reports on charge transfer on the WSe_2/MoS_2 system[54,55]; however, the momentum-resolved data collection scheme now facilitates the separate extraction of this dynamics for the intermediate Σ_W excitons.

Long-term picosecond relaxation dynamics of the observed excitons

Extended Data Fig. 9b shows the picosecond exciton relaxation dynamics of the WSe_2/MoS_2 heterostructure. In accordance with the snapshots in Extended Data Fig. 6, at 10-ps pump–probe delay, photoemission yield from the A_W exciton and the Σ_W exciton is at the detection limit of the experiment. In contrast, for the ILX, notable photoemission yield is still present at this time delay and remains beyond delays of 50 ps, which is the largest delay measured in our experiment. In Extended Data Fig. 9b, we quantify this observation and fit the relaxation dynamics of the excitons with single-exponential decays, for which we extract lifetimes of 3.1 ± 0.3 ps, 3.0 ± 0.4 ps and 33.2 ± 4.7 ps for the A_W exciton, the Σ_W exciton and the ILX, respectively. We find that the ILX lifetime is an order of magnitude larger than the lifetimes of the intralayer excitons, in agreement with earlier reports[55]. In addition, we note that the lifetimes of the intralayer excitons in the heterostructure are considerably quenched compared with the lifetime of the intralayer excitons in the WSe_2 monolayer (Fig. 2a,b), which is caused by the additional decay channel into the ILX.

Construction of the ILX momentum fingerprint in the extended zone scheme

We follow the interlayer interaction model in ref. [39] to describe the intensity distribution of the ILX fingerprint in momentum space. In Fig. 3d, we plot the measured ILX momentum distribution at 10-ps pump–probe delay together with the twisted extended zone schemes of WSe_2 (orange hexagons) and MoS_2 (dotted dark red hexagons). The K_{Mo} valleys, at which the electron contribution to the ILX is expected without contribution of the moiré superlattice, are labelled with red filled symbols. The increasing momentum distance of the K_{Mo} valleys in higher-order Brillouin zones with respect to the Γ valley of the centre Brillouin zone is indicated by the changing red symbols, that is, the

transition from circles to squares and to triangles. By umklapp scattering with the reciprocal lattice vector $\mathbf{G}^{i}_{W}$ of WSe_2 (black arrows), that is, the periodicity of the layer where the hole contribution to the ILX is localized, the momenta indicated with open symbols can be reached. As detailed in refs. [39,56], the efficiency of umklapp scattering decreases with increasing distance from the Γ valley of the centre Brillouin zone. Consequently, we observe a strong hierarchy of photoemission signal from the ILX. The strongest photoemission signal is found and expected at the momenta labelled with circles. The weaker and negligible signal is found at the momenta labelled with squares and triangles, respectively.

For heterostructures with different twist angles, the ILX momentum structure is modified accordingly. This is exemplarily illustrated in Extended Data Fig. 10 for twist angles of 9° and 2°. Here, the 2° illustration corresponds to the sample structure in a recent study[13], and shows that for finite momentum resolution and small twist angles, the ILX momentum structure that we found in our work cannot be resolved.

Real-space reconstruction

Following the plane-wave model for photoemission, the measured ARPES intensity $I(\mathbf{k})$ can be expressed as

$$I(\mathbf{k}) = |\mathbf{A}\cdot\mathbf{k}|^2 |\mathrm{FT}\{\psi(\mathbf{r})\}|^2 \delta(E_b + E_{kin} + \phi - \hbar\omega),$$

which includes the Fourier transform of the real-space electronic wavefunction $\psi(\mathbf{r})$, a polarization factor $|\mathbf{A}\cdot\mathbf{k}|^2$ that depends on the vector potential $\mathbf{A}$ of the incident radiation and electron momentum $\mathbf{k}$, and a Dirac delta function that ensures conservation of energy (E_b: binding energy, E_{kin}: kinetic energy of electrons, Φ: work function, $\hbar\omega$: photon energy). As the electronic contribution to the interlayer excitonic quasiparticle is confined to a single MoS_2 monolayer, we can treat it similar to how it is done for orbital tomography of molecular orbitals in planar aromatic molecules[40,57], in agreement with the approach that has been recently carried out for excitons in TMDs[13,28,34]. Here, the wavefunction is assumed to be thin in the vertical dimension and photoemission is therefore assumed to be independent of the out-of-plane momentum k_z.

We start our analysis based on the momentum maps of the A_W exciton and the ILX. As highlighted in the main text based on the insets in Fig. 4a,b, we perform separate two-dimensional Fourier transforms to each excitonic photoemission feature to reconstruct the real-space extension of the electronic contribution to the exciton wavefunction, as plotted in Fig. 4a,b for the ILX and the A_W exciton, respectively. In this analysis, we have eliminated broadening effects owing to the finite momentum resolution of the momentum microscope (0.04 $Å^{-1}$) using Wiener–Hunt deconvolution and subtracted a weak background determined from the full dataset. Finally, we assumed a flat phase profile over the full accessible momentum range, following the approach detailed in ref. [28]. To determine the Bohr radii, we calculate the root-mean-square radii of the real-space probability density distribution. The Bohr radii for the electron contribution to the ILX and the A_W exciton are $r_B^{ILX} = 1.6 \pm 0.2$ nm and $r_B^{A_W} = 1.1 \pm 0.1$ nm, respectively, and were acquired by taking the weighted average of the Bohr radii determined for individual κ and K_W valleys. For the ILX, only the features with a signal-to-noise ratio better than 10 were taken into account.

It is noted that on the heterostructure with a twist angle of more than 5°, we can safely assume in our analysis that the centre-of-mass momentum is narrowly distributed around zero[11,38], and the momentum width of the photoemission signatures at the κ and K_W valleys relates to the relative coordinate of the excitons[13]. In a recent report on a 2°-twisted WSe_2/MoS_2 heterostructure, ref. [13] reported the root-mean-square radius of the relative coordinate to the ILX wavefunction to 2.6 ± 0.4 nm. This corresponds to a root-mean-square radius of the probability density of 1.8 ± 0.3 nm, which is in agreement with our analysis of a Bohr radius of $r_B^{ILX} = 1.6 \pm 0.2$ nm. Similarly, our reconstructed Bohr radius of the A_W exciton of $r_B^{A_W} = 1.1 \pm 0.1$ nm is in agreement with the root-mean-square radius of the probability density of WSe_2 of ref. [34] (about 1.0 nm).

Data availability

The data that support the findings of this study are available from the corresponding authors upon reasonable request.

41. Stansbury, C. H. et al. Visualizing electron localization of WS_2/WSe_2 moiré superlattices in momentum space. *Sci. Adv.* **7**, eabf4387 (2021).
42. Tusche, C., Krasyuk, A. & Kirschner, J. Spin resolved bandstructure imaging with a high resolution momentum microscope. *Ultramicroscopy* **159**, 520–529 (2015).
43. Miaja-Avila, L. et al. Laser-assisted photoelectric effect from surfaces. *Phys. Rev. Lett.* **97**, 113604 (2006).
44. Ulstrup, S. et al. Imaging microscopic electronic contrasts at the interface of single-layer WS_2 with oxide and boron nitride substrates. *Appl. Phys. Lett.* **114**, 151601 (2019).
45. Jones, A. J. H. et al. Visualizing band structure hybridization and superlattice effects in twisted MoS_2/WS_2 heterobilayers. *2D Mater.* **9**, 015032 (2021).
46. Schönhense, G. et al. Suppression of the vacuum space-charge effect in fs-photoemission by a retarding electrostatic front lens. *Rev. Sci. Instrum.* **92**, 053703 (2021).
47. Hellmann, S., Rossnagel, K., Marczynski-Bühlow, M. & Kipp, L. Vacuum space-charge effects in solid-state photoemission. *Phys. Rev. B* **79**, 035402 (2009).
48. Passlack, S. et al. Space charge effects in photoemission with a low repetition, high intensity femtosecond laser source. *J. Appl. Phys.* **100**, 024912 (2006).
49. Chernikov, A., Ruppert, C., Hill, H. M., Rigosi, A. F. & Heinz, T. F. Population inversion and giant bandgap renormalization in atomically thin WS_2 layers. *Nat. Photon.* **9**, 466–470 (2015).
50. Dendzik, M. et al. Observation of an excitonic mott transition through ultrafast core-cum-conduction photoemission spectroscopy. *Phys. Rev. Lett.* **125**, 096401 (2020).
51. Steinleitner, P. et al. Direct observation of ultrafast exciton formation in a monolayer of WSe_2. *Nano Lett.* **17**, 1455–1460 (2017).
52. Steinhoff, A. et al. Exciton fission in monolayer transition metal dichalcogenide semiconductors. *Nat. Commun.* **8**, 1166 (2017).
53. Liu, F., Ziffer, M. E., Hansen, K. R., Wang, J. & Zhu, X. Direct determination of band-gap renormalization in the photoexcited monolayer MoS_2. *Phys. Rev. Lett.* **122**, 246803 (2019).
54. Zimmermann, J. E. et al. Ultrafast charge-transfer dynamics in twisted MoS_2/WSe_2 heterostructures. *ACS Nano* **15**, 14725–14731 (2021).
55. Zhu, H. et al. Interfacial charge transfer circumventing momentum mismatch at two-dimensional van der Waals heterojunctions. *Nano Lett.* **17**, 3591–3598 (2017).
56. Ahn, S. J. et al. Dirac electrons in a dodecagonal graphene quasicrystal. *Science* **361**, 782–786 (2018).
57. Jansen, G. S. M. et al. Efficient orbital imaging based on ultrafast momentum microscopy and sparsity-driven phase retrieval. *New J. Phys.* **22**, 063012 (2020).

Acknowledgements This work was funded by the Deutsche Forschungsgemeinschaft (DFG, German Research Foundation) - 432680300/SFB 1456, project B01, 217133147/SFB 1073, projects B07 and B10, and 223848855/SFB 1083, project B9. G.S.M.J. acknowledges financial support by the Alexander von Humboldt Foundation. A.A. and S.H. acknowledge funding from EPSRC (EP/T001038/1, EP/P005152/1). A.A. acknowledges financial support by the Saudi Arabian Ministry of Higher Education. K.W. and T.T. acknowledge support from the Elemental Strategy Initiative conducted by the MEXT, Japan (Grant Number JPMXP0112101001) and JSPS KAKENHI (grant numbers 19H05790, 20H00354 and 21H05233). E.M. acknowledges support from the European Union Horizon 2020 research and innovation programme under grant agreement number 881603 (Graphene Flagship) as well as Vinnova via the competence centre '2D-TECH' and the Knut and Alice Wallenberg Foundation via the Grant KAW 2019.0140.

Author contributions D. Steil, R.T.W., S.S., G.S.M.J., S.H., M.R. and S.M. conceived the research. D. Schmitt, J.P.B. and W.B. carried out the time-resolved momentum microscopy experiments and analysed the data. W.B., D.R.L. and G.S.M.J. carried out the real-space reconstruction of the momentum fingerprints. A.A. fabricated the samples. G.M., S.B. and E.M. developed the microscopic model and analysed the results. All authors discussed the results. M.R. and S.M. were responsible for the overall project direction and wrote the manuscript with contributions from all co-authors. K.W. and T.T. synthesized the hBN crystals.

Competing interests The authors declare no competing interests.

Additional information

Supplementary information The online version contains supplementary material available at https://doi.org/10.1038/s41586-022-04977-7.

Correspondence and requests for materials should be addressed to Marcel Reutzel or Stefan Mathias.

Peer review information *Nature* thanks Alessandra Lanzara, Simone Latini and Soren Ulstrup for their contribution to the peer review of this work.

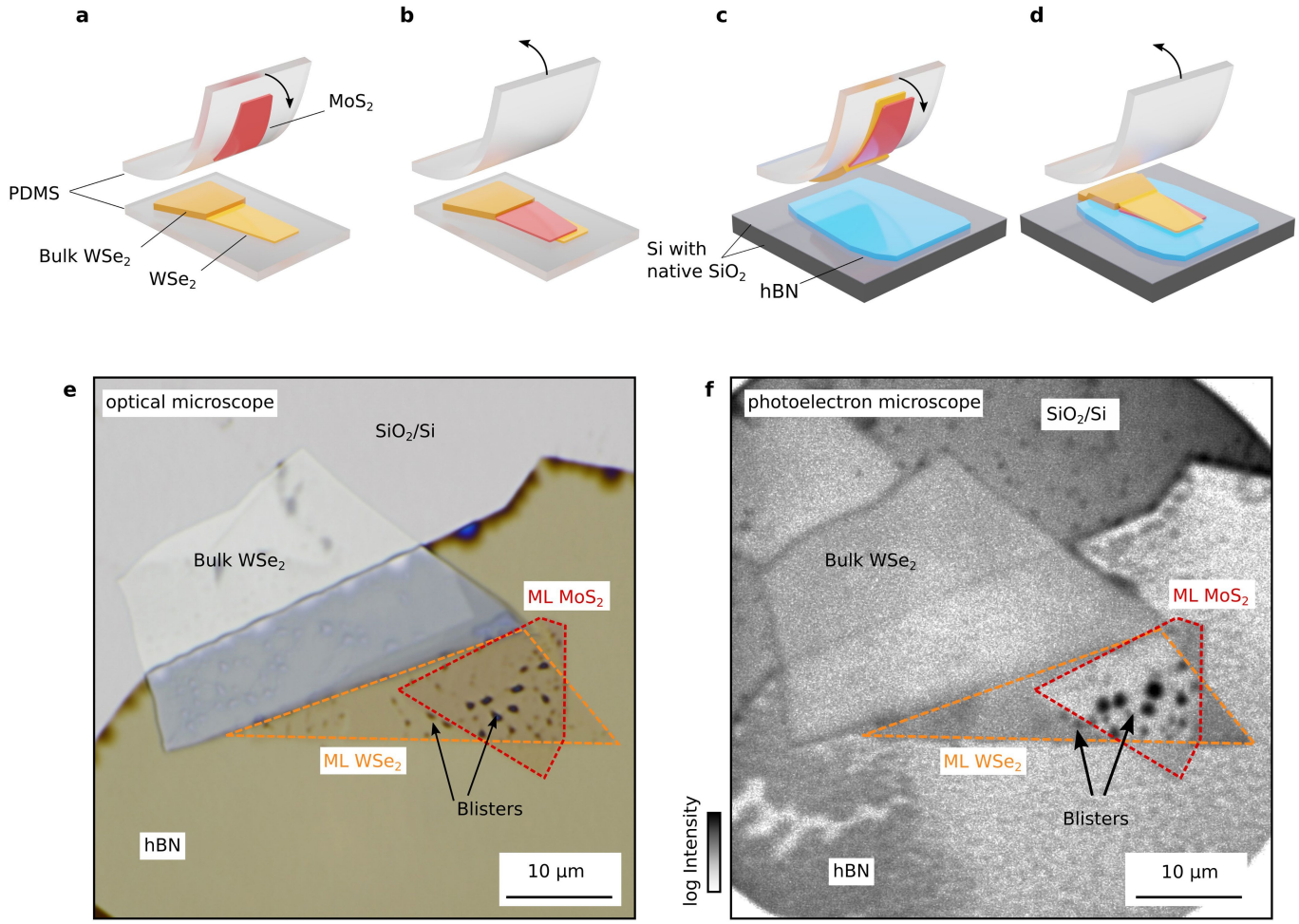

Extended Data Fig. 1 | Fabrication and real-space imaging of the of the WSe_2/MoS_2/hBN heterostructure. a–**d** Schematic of the WSe_2/MoS_2/hBN heterostructure assembly on a Si substrate with a native oxide layer. **a** A PDMS stamp with monolayer MoS_2 flake (red) is aligned with another PDMS stamp holding a monolayer WSe_2 (yellow), then the top PDMS stamp is brought in contact with bottom PDMS. **b** The top PDMS stamp is then withdrawn, leaving the MoS_2 on top of the WSe_2. **c** The PDMS stamp holding the WSe_2/MoS_2 is then brought into contact with SiO_2/Si substrate with hBN (blue). **d** the PDMS is then withdrawn, leaving behind the final WSe_2/MoS_2/hBN heterostructure. **e**/**f** The WSe_2/MoS_2/hBN heterostructure, the uncovered SiO_2/Si substrate, bulk hBN, the WSe_2 and MoS_2 monolayers, and bulk WSe_2 are labelled in the **e** optical microscope and the **f** photoemission real-space image ($\hbar\omega = 4.96$ eV). Point-like structures (blisters) in the heterostructure region can be attributed to residual gas trapped either at the MoS_2/hBN or the WSe_2/MoS_2 interface. The blisters in the monolayer WSe_2 region are most likely trapped at the WSe_2/hBN interface.

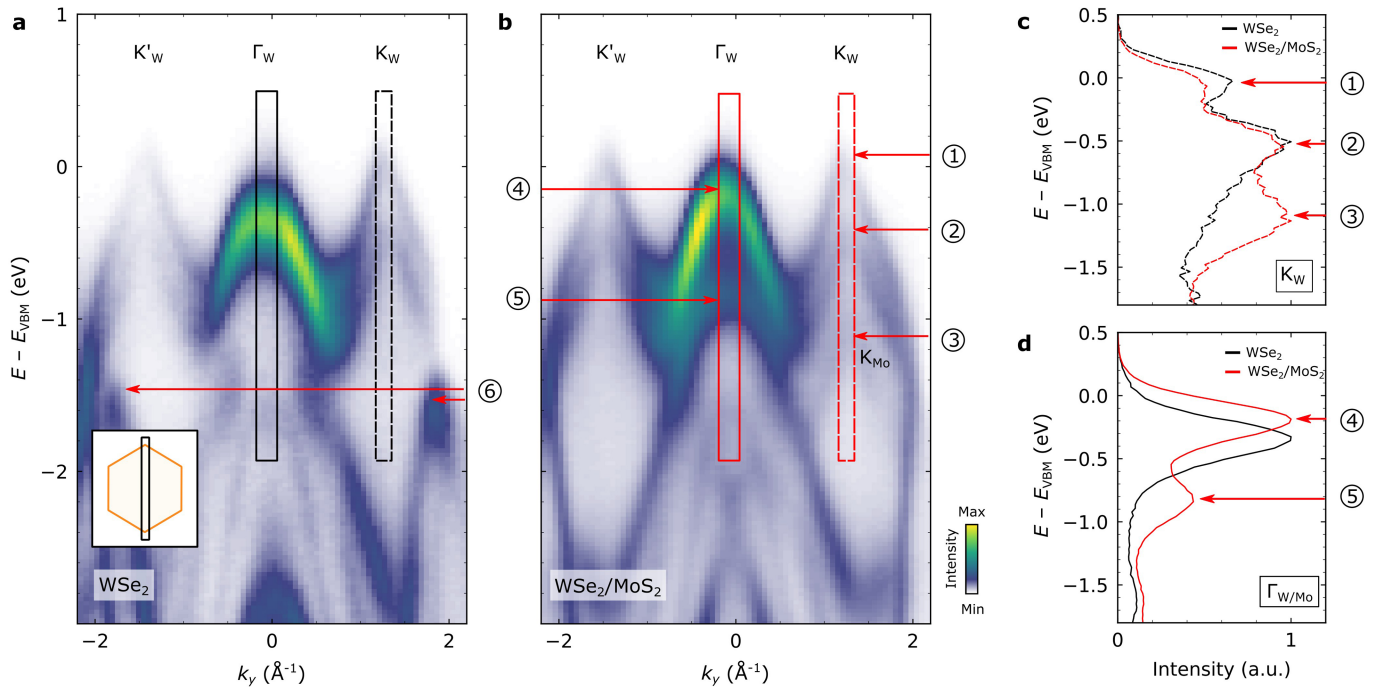

Extended Data Fig. 2 | Static band mapping of the monolayer WSe_2 and the heterobilayer WSe_2/MoS_2. a,b Energy–momentum representation of the static photoemission intensity obtained in the momentum microscopy experiment along the K'_W-Γ-K_W direction (see inset). The important spectroscopic features are labelled in the figure: (1, 2) spin-split valence bands of WSe_2; (3) valence band of MoS_2; (4, 5) valence bands at the $\Gamma_{W,Mo}$ valley; (6) valence band of hBN. **c, d** Energy-distribution curves taken around the K_W and $\Gamma_{W,Mo}$ (Γ_W) valley indicated by the coloured boxes in **a** and **b**.

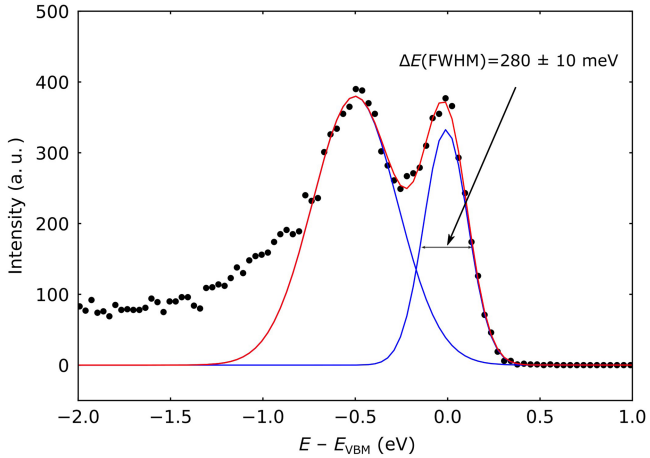

Extended Data Fig. 3 | Inhomogeneous broadening of the photoemission spectra. The energy-distribution-curve is obtained in a ± 0.10 $Å^{-1}$ region-of-interest centred at the K'_W valley of WSe_2. Gaussian fitting of the valence band maximum centred at E-E_{VBM} = 0 eV yields a full-width at half-maximum of 280 ± 10 meV.

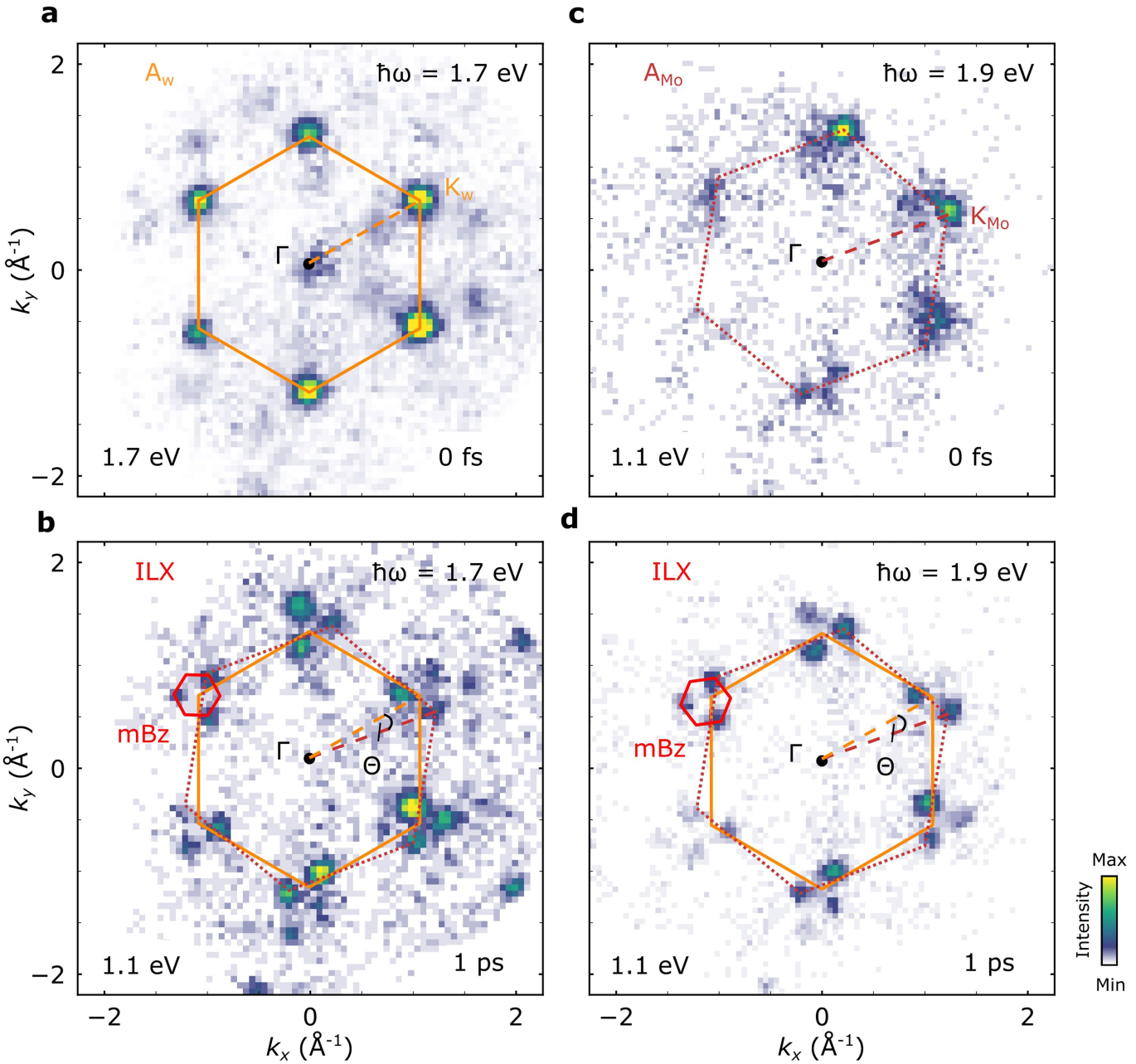

Extended Data Fig. 4 | Determination of the twist angle Θ of the WSe_2/MoS_2 heterostructure. The momentum maps in **a** and **c** show the photoemission fingerprint of the A_W- and A_{Mo}-excitons when excited resonantly with 1.7 eV and 1.9 eV photons, respectively, at 0 fs pump–probe delay. Since the MoS_2 A_{Mo}-exciton and the ILX are, within our energy resolution, spectrally degenerate, faint signatures of the ILX are already visible **c** at 0 fs delay. The dashed lines indicate the Γ-K_W (orange) and Γ-K_{Mo} (dark red) direction. From their misalignment, the twist angle is extracted to Θ = 9.8 ± 0.8°. **b**, **d** At 1-ps pump–probe delay, the ILX momentum fingerprint can be identified, as described by the mBZ (red). The dashed lines indicate the relation of the ILX momentum fingerprint and the Γ-K_W and Γ-K_{Mo} directions. Note the distinctly different intensity distribution of the combined spectral weight of the A_{Mo}-exciton and the faint ILX in **c** vs. the pure signature of the ILX at 1-ps delay in **d**. For each momentum-map, the photoelectron energy with respect to the valence band maximum of WSe_2 and the pump–probe delay are noted in the lower left and right corner, respectively.

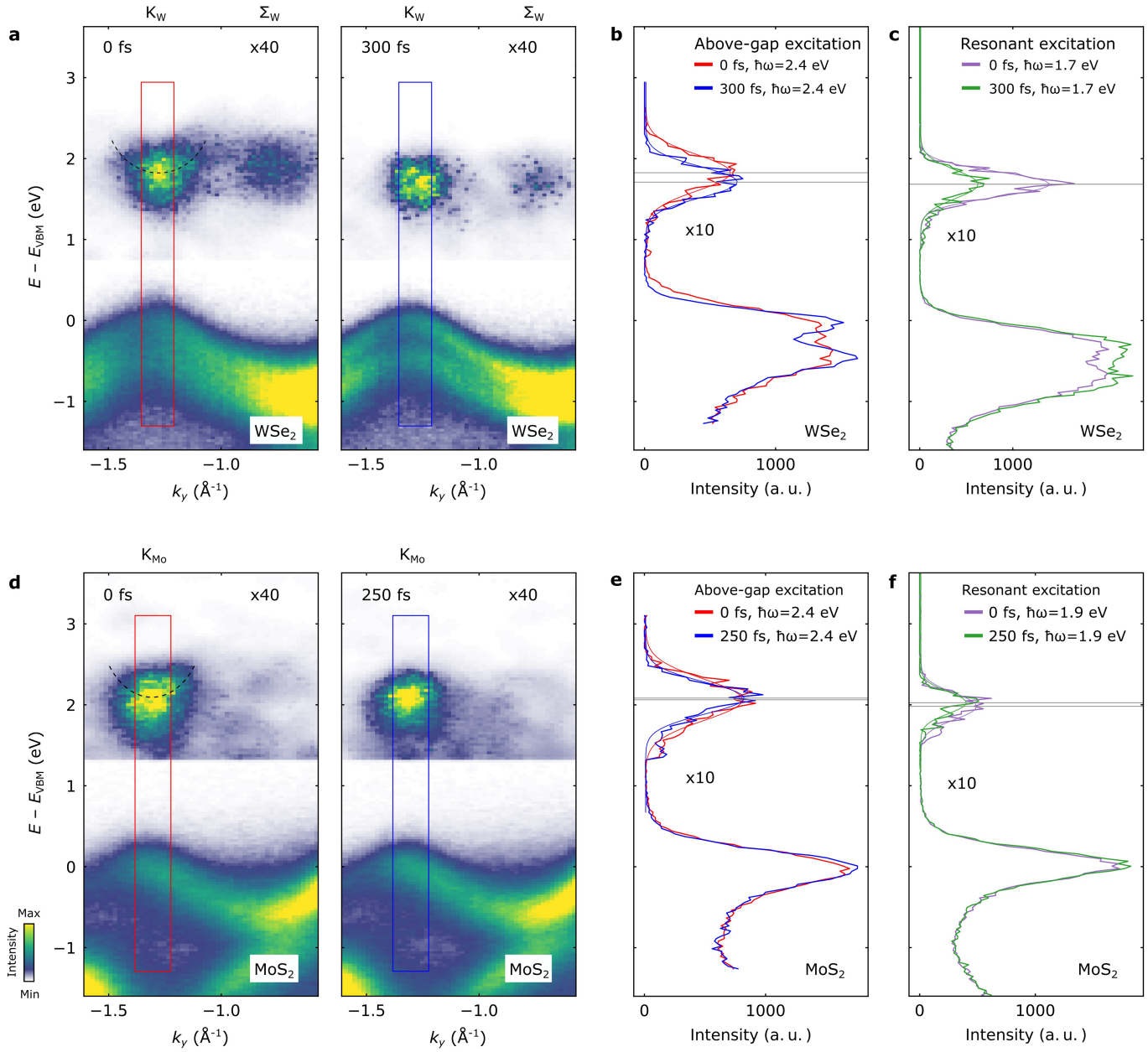

Extended Data Fig. 5 | Above-band-gap excitation of monolayer WSe_2 and monolayer MoS_2. Photoemission yield from bright intralayer excitons and charge carriers in the conduction can be discriminated based on above-band-gap excitation data collected on **a**–**c** monolayer WSe_2 (orange circle in Fig. 1c) and **d**–**f** monolayer MoS_2 (real-space image not shown). **a** and **d** show energy–momentum cuts along the K-Σ direction measured on WSe_2 and MoS_2, respectively, at 0 fs and 300 fs (respectively 250 fs) pump–probe delay. At 0 fs, a parabolic signature with positive dispersion is detected at the K valley (noted by the black dashed parabolic line). At 300 fs (250 fs), the signature becomes more spherical. **b** and **e** show energy-distribution curves at the K valleys (momentum-integration region based on the boxes in **a, d**). The peak maxima is indicated by grey horizontal lines. **c** and **f** show the corresponding energy-distribution curves when excited on resonance with the A_W- and A_{Mo}-exciton, respectively.

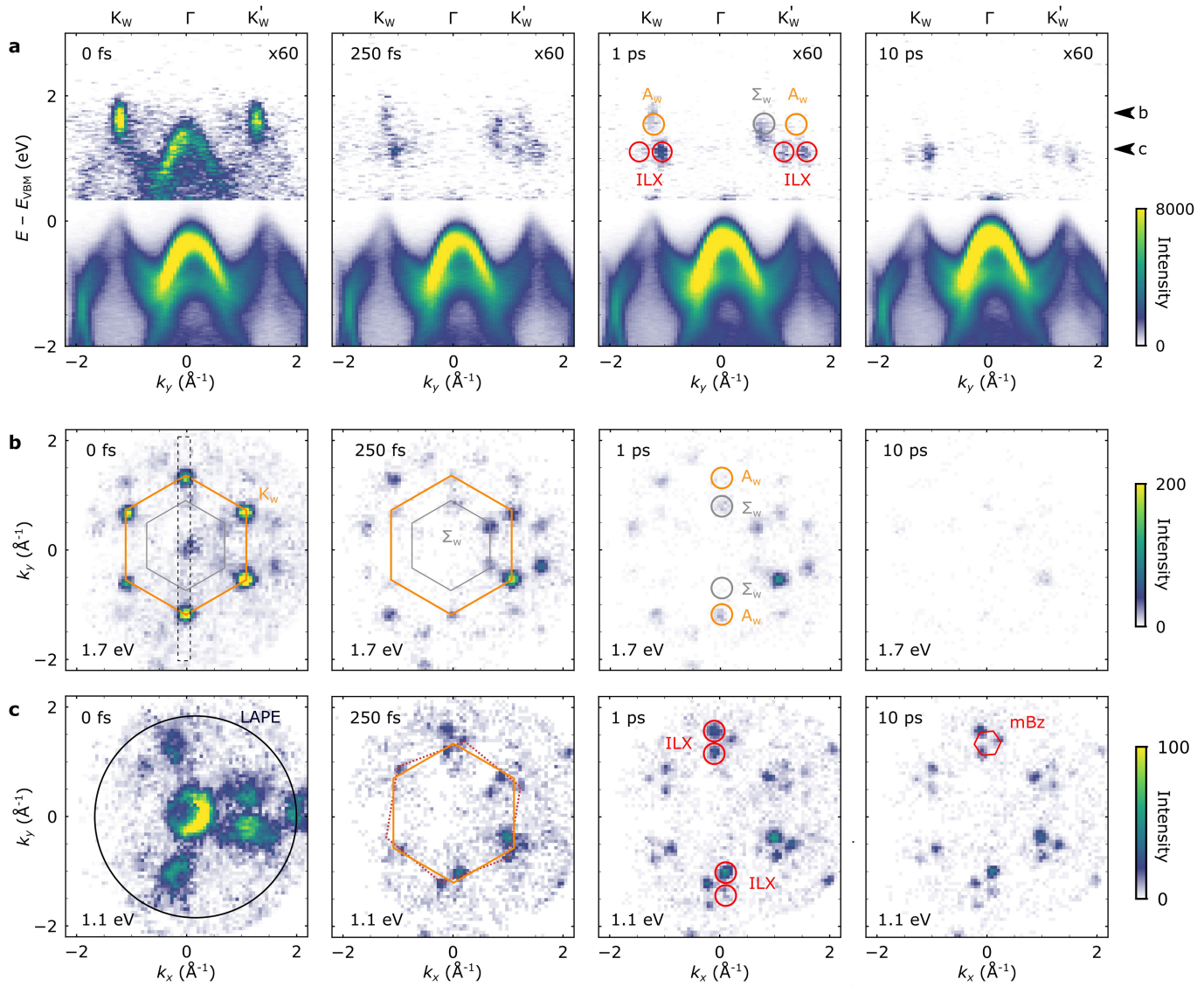

Extended Data Fig. 6 | Additional trARPES data of the ILX formation. a E(*k*) cut along the K_W-Γ-K'_W direction integrated in the *k*-region shown by the black dashed box in **b**, 0 fs. The arrowheads on the right side of the figure indicate the photoelectron energies where the momentum maps in **b** and **c** are centred. **b** Within the energy window of the k-map (E-E_{VBM} = 1.7 eV) and increasing pump–probe delay, spectral weight from the bright A_W-excitons (orange hexagon) is transferred via exciton–phonon scattering to form dark Σ_W-excitons (grey hexagon). **c** Interlayer charge transfer via the Σ-valleys forms the ILX, which is observed at E-E_{VBM} = 1.1 eV. The Brillouin zone of MoS_2 is indicated with a dotted dark red hexagon and the mBZ with a red hexagon. Spectroscopic signatures of the A_W-exciton, the Σ_W-exciton, and the ILX are indicated by orange, grey, and red circles, respectively, in the 1 ps data. The pump–probe delay and the binding energy of the k-maps are noted in the top and bottom left corner, respectively. Note that at 0 fs, the strong signal in **c** is mainly caused by LAPE. In addition, in **b** (0 fs), LAPE leads to photoemission yield at the Γ point.

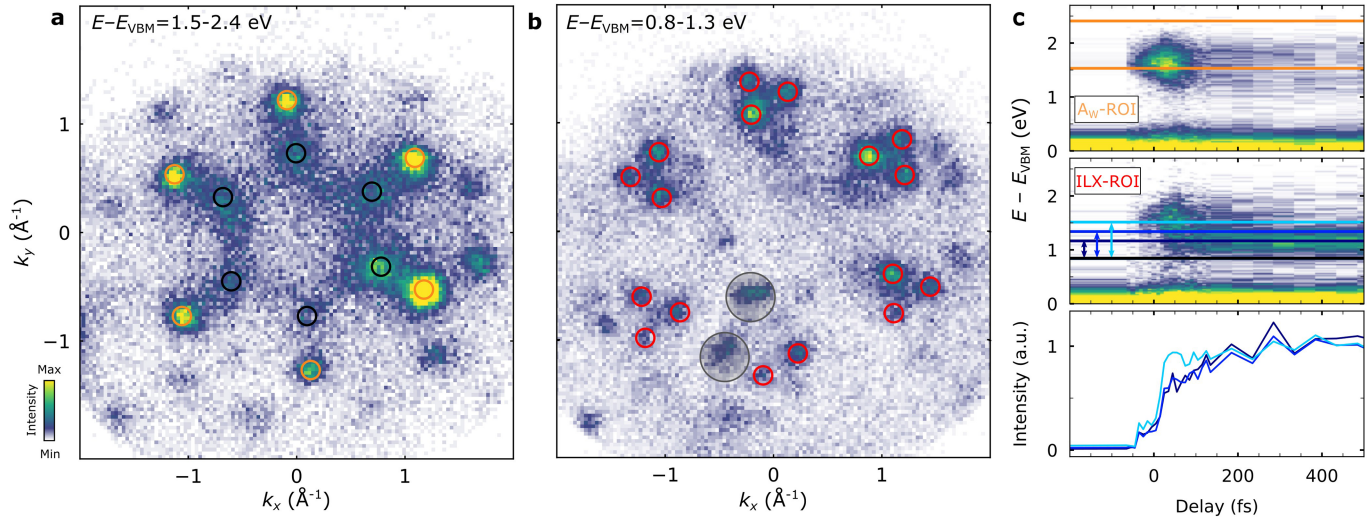

Extended Data Fig. 7 | Selected regions of interest for the analysis of the A_W-, Σ_W-, and ILX formation dynamics shown in Fig. 2c. a and **b** show momentum maps integrated over all measured pump–probe delays in the energy intervals of E-E_{VBM} = 1.5–2.4 eV and 0.8–1.3 eV, respectively. The regions-of-interest that are used for filtering the excitonic photoemission signatures in momentum space are indicated by orange, black, and red circles for the A_W-exciton, the Σ_W-exciton, and the ILX, respectively. The grey shaded areas indicate artefacts of the detector. **c** (top and middle panel) Pump–probe delay evolution of the energy- distribution curves filtered for the orange and red regions of interest. **c** (bottom panel) Intensity vs. pump–probe delay plots for the energy boxes indicated by the bluish arrows in the middle panel.

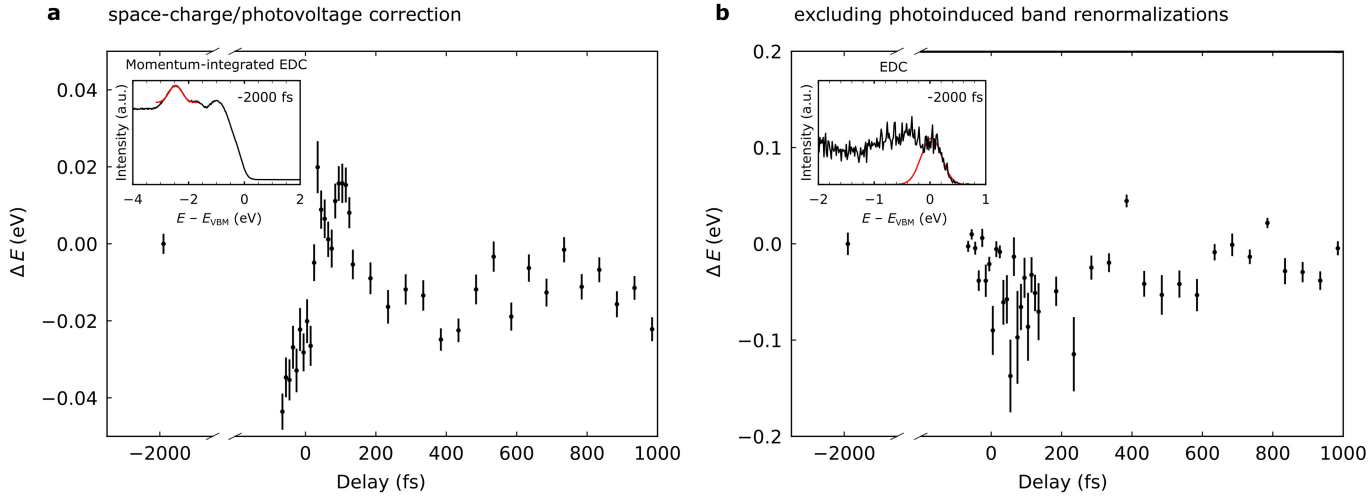

Extended Data Fig. 8 | Correction of space-charge/photovoltage-induced shifts and exclusion of photoinduced band renormalizations. a The rigid band shift ΔE of maximal 70 meV is corrected for each pump–probe delay. ΔE is obtained by fitting (red) momentum-integrated energy-distribution curves (black) for each delay, as exemplary shown for the −2000 fs measurement in the inset. The error bars are standard deviations obtained in each fit. **b** We fit the pump–probe delay-dependent energetic peak position of the valence band maximum of WSe_2 at the K_W valley with Gaussian distributions (red, inset) and calculate the energy difference ΔE with respect to the −2000 fs measurement that is plotted in the inset. Within the scattering of the data, ΔE does not upshift with pump–probe delay, excluding a dominant contribution of photoinduced band renormalization such as discussed in refs. [49,53].

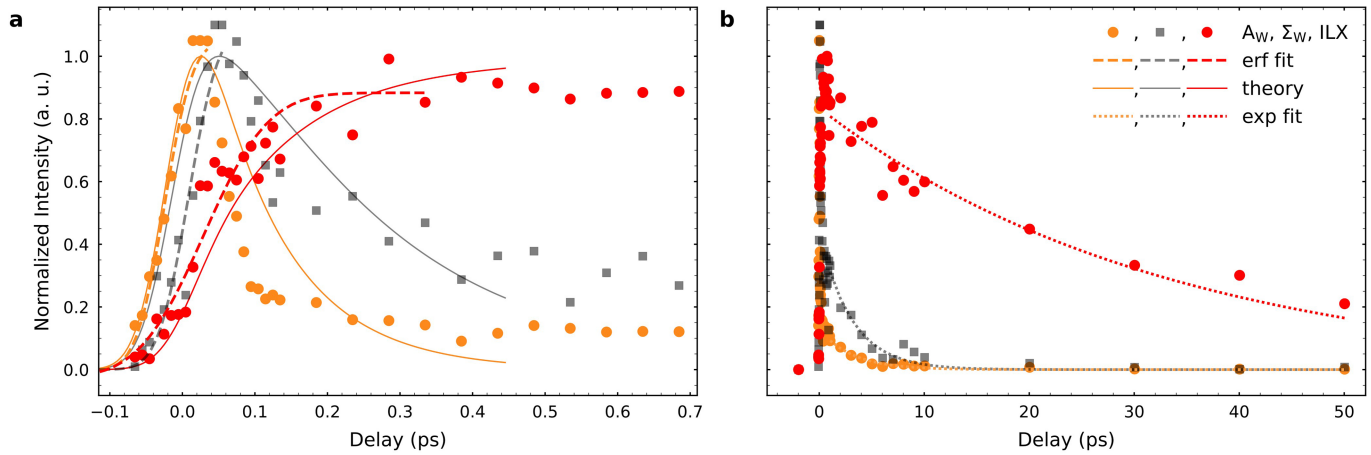

Extended Data Fig. 9 | Charge-transfer and charge recombination times of the A_W exciton (orange), the Σ_W exciton (grey), and the ILX (red). a The short-time dynamics (symbols) is fitted with error functions (dashed lines), from which the delayed onset times t_i are extracted, as detailed in the text. The solid lines reproduce the model calculations initially shown in Fig. 2c of the main text. **b** The charge recombination time is extracted by performing single-exponential fits to the data for pump–probe delays larger than 1 ps.

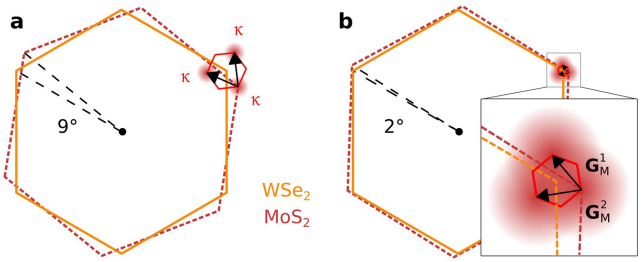

Extended Data Fig. 10 | Sketch of the moiré mBz for small and large twist angles. The twist angle Θ defines the size of the moiré mBz (red hexagon) and the related moiré reciprocal lattice vectors $G^{1,2}_{M}$ (black arrows). **a** For twist angles larger than a few degree, $G^{1,2}_{M}$ is larger than the momentum width of a single κ valley (dark reddish filled circles). All three κ valleys (and higher-order umklapp processes) are detected in the momentum microscopy experiment (Fig. 3c, d). The electronic contribution to the ILX wavefunction is spread across several moiré potential wells (Fig. 4). **b** For sufficiently small twist angles, $G^{1,2}_{M}$ can become smaller than the width of a single κ valley, and the ILX wavefunction can be confined in a single moiré potential well. If the momentum microscopy experiment is performed with a finite momentum resolution, the photoelectron signal from the ILX can appear as a single peak, as reported in Ref. [13] for a 2° twisted WSe_2/MoS_2 heterostructure.